

X-ray Detection from Bona-fide and Candidate Brown Dwarfs in the ρ Ophiuchi Cloud with *Chandra*

Kensuke Imanishi, Masahiro Tsujimoto, and Katsuji Koyama

Department of Physics, Graduate School of Science, Kyoto University, Sakyo-ku, Kyoto, 606-8502, Japan

kensuke@cr.scphys.kyoto-u.ac.jp, tsujimot@cr.scphys.kyoto-u.ac.jp,

koyama@cr.scphys.kyoto-u.ac.jp

ABSTRACT

We present results of an X-ray search from bona-fide and candidate brown dwarfs in the ρ Ophiuchi cloud cores with the *Chandra* X-ray Observatory. The selected areas are two fields near the cloud center and are observed with the ACIS-I array of a $17' \times 17'$ size and a ~ 100 ks exposure. Among 18 bona-fide and candidate brown dwarfs listed by the infrared spectroscopy, we find X-ray emission from 7 sources above 99.9% confidence level. Therefore $\sim 40\%$ of the infrared-selected brown dwarfs in this cloud emit X-rays. For the brightest 4 sources, the X-ray spectra are made and are fitted with a thin-thermal plasma model of a temperature 1–2.5 keV. The X-rays are also time variable with rapid flares from 2 of the brown dwarfs. Assuming 2 keV temperature and using the empirical relation of A_V vs. N_H , we estimate the X-ray luminosity or its upper limit of the other faint or non-X-ray sources. The X-ray luminosity (L_X) of the X-ray-detected sources is in the range of $0.3\text{--}90 \times 10^{28}$ ergs s $^{-1}$, while the luminosity ratio of X-ray to bolometric (L_X/L_{bol}) is $10^{-3}\text{--}10^{-5}$, similar to those of low-mass pre-main-sequence and dMe stars. All these results suggest that the X-ray origin of brown dwarfs is the same as low-mass stars; strong magnetic activity at the stellar surface.

Subject headings: stars: low-mass, brown dwarfs — X-rays: stars — ISM: individual (ρ Ophiuchi cloud)

1. INTRODUCTION

Brown dwarfs are sub-stellar objects with mass well below the hydrogen burning limit ($\sim 0.08 M_\odot$), which fill up the gap between stars and planets. With no stable nuclear burning, the energy source of brown dwarfs is gravitational contraction, hence brown dwarfs become cooler and less luminous with the increasing ages. *ROSAT* detected X-rays from several brown dwarfs and their candidates in star-forming regions; Chamaeleon, ρ Ophiuchi (ρ Oph), and Taurus (Neuhäuser & Comrérón 1998; Neuhäuser et al. 1999). X-ray flares from field brown dwarfs were also found (Fleming, Giampapa, & Schmitt 2000; Rutledge et al. 2000). These X-ray features are similar to those of low-mass stars, hence the X-rays are likely to be magnetic origin. However the standard (α - ω) dynamo to produce the magnetic

activity may not present, because brown dwarfs are fully convective, hence there are no anchor points of the magnetic field in the star interior (Drake et al. 1996). In order to address the X-ray features and to study the emission mechanisms of brown dwarfs, our current knowledge is still very poor, due mainly to the limited sensitivity of the previous instruments. This observational constrain is largely relaxed by the *Chandra* X-ray Observatory of wide band sensitivity (0.5–10.0 keV) coupled with unprecedented spatial resolution of $\sim 0.5''$ (Weisskopf, O'dell, & van Speybroeck 1996). We systematically search and study X-rays from brown dwarfs in one of the nearest star-forming regions, using the data of two deep ACIS-I exposures on the ρ Oph molecular cloud cores.

2. OBSERVATIONS AND DATA REDUCTION

Two *Chandra* observations were made on the central region of the ρ Oph cloud with the ACIS-I array consisting of four abutted X-ray CCDs. The first observation (here and after, obs.1) covered a $17'.4 \times 17'.4$ area including cores B, C, E, and F, while the second observation (obs.2) covered the center of core A (Motte, André, & Neri 1998). The level 2 data are retrieved from the *Chandra* X-ray Center (CXC) archive, in which the data degradation caused by the increase of charge transfer inefficiency (CTI) in orbit is corrected. X-ray events are selected with the *ASCA* grades 0, 2, 3, 4, and 6. After the processing, ≈ 100 ks effective exposure time is obtained from each observation. The log of the observations is listed in Table 1.

In these two fields, 18 late M dwarfs have been reported, based on the water vapor absorption at $\lambda = 2.4\text{--}2.5 \mu\text{m}$ (Wilking, Greene, & Meyer 1999; Cushing, Tokunaga, & Kobayashi 2000). Among them, 8 sources have the upper limit of mass less than $0.08 M_{\odot}$, which we call “bonafide brown dwarfs” (here and after, BDs). The other 10 sources have a mass in the transition region of $0.08 M_{\odot}$, hence called “candidate brown dwarfs” (CBDs). Their names and spectral types are shown in Table 2.

3. ANALYSIS AND RESULTS

3.1. Source Detection

Using the `wavdetect`¹ command, we pick up ~ 100 X-ray sources from each field above the significance criterion of 10^{-7} . Infrared (IR) counterparts from the catalog of Barsony et al. (1997) are searched and the position is cross-correlated to that of the X-ray source. Systematic coordinate offset of the *Chandra* frame is then fine-tuned to fit the IR frame. After the offset correction, the relative position error (1σ) is $1''.2$. We find X-ray counterparts from 5 IR positions in a 2σ error radius ($2''.4$) out of the 18 catalogued BDs and CBDs (GY 310, GY 31, GY 37, GY 59, and GY 326). The X-ray positions and relative offsets from the IR sources are given in Table 2. The X-ray counts

are extracted from a circle of a half radius of the point-spread function (PSF) around the X-ray position.

Since no apparent X-ray sources are found in a 2σ error radius ($2''.4$) of the other 13 catalogued BDs and CBDs, we define a circle with a half radius of PSF around each IR position. Then we manually count the X-ray photons in the circle. We note that a rather small source radius is selected so as to maximize the signal-to-noise (S/N) ratio, particularly, for faint X-ray sources. Nevertheless, as is demonstrated in the 5 bright sources, the position error between IR and X-rays is always smaller than the source radius, because both have generally similar dependence on the source off-axis angle; both have the smaller values for the sources with smaller off-axis angle. Therefore most of the X-ray photons for the relevant BDs and CBDs, if any, may fall in the source circles. The X-ray flux thus counted are given in Table 2.

The mean background counts are estimated from source-free regions of a 63-arcmin^2 and a 59-arcmin^2 area in the ACIS-I fields for obs.1 and obs.2, respectively. The soft band (0.5–2.0 keV) background counts (in units of 10^{-2} counts arcsec^{-2}) are 2.3 and 2.2, for obs.1 and obs. 2, respectively, while those in the hard (2.0–9.0 keV) band are about 3 times larger, 6.8 and 6.5 for obs.1 and obs. 2. The background counts in each source area are given in Table 2. We then separately calculate the confidence level (CL) of the X-ray detection for the soft, hard and total (0.5–9.0 keV) bands. Based on the Poisson statistics, the CL is defined as;

$$CL = \sum_{N'=0}^{N_0-1} e^{-N_{bg}} \frac{N_{bg}^{N'}}{N'!}$$

where N_0 and N_{bg} are the detected and the background counts in the source circle, respectively (see e.g., Gehrels 1986, and references therein). We set the detection (or the upper limit) criterion that the CL should be larger than 0.999 ($\approx 3.3\sigma$) in any of the 3 energy band data. In Table 2, we show the maximum CL value for each source. For sources located in both fields of view (GY 141, GY 163, and GY 202), we also estimate the CL for the combined data as well as the separate data. However, no higher CL value is obtained from all the sources.

¹see <http://asc.harvard.edu/udocs/docs/swdocs/detect/html/>

As are summarized in Table 2, bright X-rays are found from 3 CBDs (GY 31, GY 37, and GY 59) in addition to previously reported sources, GY 310 and GY 326 (Imanishi, Tsuboi, & Koyama 2001). Detection of X-rays from a CBD, GY 84 is also highly significant. Another BD, GY 141 in obs.1, show faint X-rays with CL of ≥ 0.999 in the soft band. Using the $\log N$ – $\log S$ relation by Mushotzky et al. (2000), we estimate the chance coincidence of a background source to fall in the source circle to be 0.6–1 %, where the uncertainty mainly comes from the ambiguity of the amount of interstellar absorption. Furthermore, background sources are most likely AGNs and may have harder spectra than the possible counterpart of GY 141. We thus conclude that the faint X-rays from this BD are real.

3.2. X-ray Spectra and Luminosities

For the brightest 4 sources —, 1 BD (GY 310) and 3 CBDs (GY 31, GY 59, and GY 326) —, we analyze the time-averaged X-ray spectra. The background spectra are extracted from the same regions used in §3.1. We then fit the spectra with a thin-thermal plasma (MEKAL: Mewe, Gronenschild, & van den Oord 1985) model, in which the metal abundance is fixed to 0.3 solar based on the fitting results of other *Chandra* X-ray sources in this region (Imanishi et al. 2001). The spectra and the best-fit parameters are shown in Figure 1 and Table 3. The best-fit plasma temperature (kT) is in the range of 0.9–2.5 keV. Small differences in the parameters of GY 310 and GY 326 from those in Table 1 of Imanishi et al. (2001), which is nevertheless unimportant, would be attributed to the more elaborated data-reduction process of this paper (see §2 in Imanishi et al. 2001).

For the faint or non-X-ray sources, the spectrum is assumed to be a thin-thermal plasma of 2-keV temperature (the mean value for the bright sources), while the absorption column is estimated from the empirical relation, $N_H = 1.59 \times 10^{21} A_V \text{ cm}^{-2}$ (Imanishi et al. 2001), where A_V is the visual extinction derived from IR photometry (Wilking et al. 1999; Cushing et al. 2000). We then calculate the X-ray luminosities or those of the 99.9 % upper limits in the soft band (Table 2).

3.3. Time Variability

Figure 2 shows the light curves of (a) GY 310, (b) GY 31, (c) GY 59, and (d) GY 326 in 0.5–9.0 keV, where the background levels are represented by the dashed lines. For GY 31 and GY 59, clear flare-like events, typical to those of low-mass main-sequence and pre-main-sequence stars; a fast rise and slow decay, are seen. The flare-decay timescale ($\sim 10^4$ sec) is also the same as that of low-mass stars.

GY 310 and GY 326, on the other hand, show no clear flare, but exhibit aperiodic variability of flux change by a factor of ~ 2 within 100 ks exposure. Since we see no large intensity variation in the background flux, we conclude that the variability is highly significant.

In order to search for spectral change during the flare, we separately make and fit the spectra of GY 31 in the flare and quiescent phases. A hint of spectral hardening during the flare is found, although it is not significant from the statistical point of view; kT is $2.5^{+0.9}_{-0.7}$ keV at the first flare then decreases to $2.1^{+0.6}_{-0.5}$ keV in a rather quiescent phases.

4. DISCUSSION

We detect X-ray emission from 2 out of 8 BDs and 5 out of 10 CBDs in the ρ Oph cloud cores. The X-ray detection rate is thus 25% (BD) and 50% (CBD). Neuhäuser et al. (1999) claimed the X-ray detection of only 1 BD (GY202) with *ROSAT*/PSPC, in the same fields of the present observations. Our present observations find no X-ray from GY202 with an upper limit of $1.2 \times 10^{28} \text{ ergs s}^{-1}$. Instead, we find a class I candidate WL 1 (No.13, in Imanishi et al. 2001) within the PSPC error circle of GY202. This source emits X-rays with comparable luminosity to that of GY202 reported with *ROSAT*/PSPC. Conversely, Neuhäuser et al. (1999) found no X-ray with an upper limit of $\sim 10^{28} \text{ ergs s}^{-1}$ from all the *Chandra* detected sources. They, however, estimated the X-ray luminosity assuming $kT = 1$ keV and $A_V =$ a few mag (i.e., $N_H =$ a few $\times 10^{21} \text{ cm}^{-2}$), which may be significantly lower than the real case (see Table 3). We hence re-estimate the upper limit with the same assumption adopted in this paper (§3.2), then find that the *ROSAT* upper limit could be nearly one or two order magnitude higher

than those of the original paper. If we adopt these newly estimated upper limits, we find no significant flux change from the *ROSAT* to the *Chandra* era.

In Table 2, we display the ratio of the X-ray (L_X) and bolometric (L_{bol}) luminosities. L_{bol} is roughly proportional to the area of the photosphere, hence L_X/L_{bol} is a good indicator of coronal X-ray activity per unit surface area. The L_X/L_{bol} value lies between 10^{-3} – 10^{-5} , which is similar to low-mass pre-main-sequence stars (e.g., Imanishi et al. 2001) and dMe stars (Giampapa et al. 1996), but is significantly higher than that of the quiescent solar corona; $\sim 5 \times 10^{-7}$ (Vaiana & Rosner 1978). It should also be noted that most of the upper limits of L_X/L_{bol} of X-ray non-detected BDs and CBDs are scattered around 10^{-3} – 10^{-5} , which are comparable with or slightly lower than those of X-ray detected BDs and CBDs. This leads us to suspect that these X-ray non-detected BDs and CBDs may emit X-rays below but near at the current sensitivity limit of *Chandra*.

We also obtain the X-ray spectra from 1 BD and 3 CBDs for the first time (§3.2), which are fitted with a thin thermal plasma model of ~ 2 keV temperature. Solar-like flares are also detected from 2 CBDs (GY 31 and GY 59, §3.3). These X-ray features are similar to those of low-mass stars. Together with the high L_X/L_{bol} value, we suggest that X-rays from BDs and CBDs are attributable to magnetic activities like low-mass stars. Detection of highly variable radio emission from GY 31, which probably arises from non-thermal gyro-synchrotron emission, also indicates the existence of strong and time variable magnetic activity (P. André, private communication; see Neuhäuser et al. 1999).

One debatable issue is the mechanism of magnetic field amplification. Brown dwarfs are fully convective, hence the standard dynamo (α - ω dynamo) mechanism may not work. This situation is the same as low-mass protostars. As one possible scenario, Montmerle et al. (2000) proposed an amplification of the magnetic field between the star and the circumstellar disk by twisting through the differential rotation. If BDs and CBDs emit X-rays with the same mechanism, X-ray activity should vanish when the circumstellar disk disappears as the star evolves. Figure 3 shows the relation between the excess emission at K -band and

the L_X/L_{bol} value. The excess emission is defined as $r_k = F_{K_{\text{ex}}}/F_K$, where $F_{K_{\text{ex}}}$ is the flux from excess (circumstellar) emission and F_K is the stellar flux at K -band (Willing et al. 1999; Cushing et al. 2000), hence $r_k > 0$ indicates the presence of the circumstellar disk. X-ray detected BDs and CBDs are uniformly distributed over two regions of $r_k > 0$ and $r_k \leq 0$; we see no hint that X-ray activity decreases as the circumstellar disk disappears ($r_k \leq 0$). We therefore conclude that the existence of the disk is not the key parameter in X-ray emission of BDs and CBDs. Another type of dynamo, such as turbulent-driven (α^2) dynamo (Durney, De Young, & Roxburgh 1993), is conceivable.

The authors express their thanks to Dr. Thomas Preibisch for critical refereeing and useful comments. The authors also acknowledge Dr. Yohko Tsuboi and Jun Yokogawa for useful discussions and comments. K.I. and M.T. are financially supported by JSPS Research Fellowship for Young Scientists.

REFERENCES

- Barsony, M., Kenyon, S. J., Lada, E. A., & Teuben, P. J. 1997, *ApJS*, 112, 109
- Cushing, M. C., Tokunaga, A. T., & Kobayashi, N. 2000, *AJ*, 119, 3019
- de Zeeuw, P. T., Hoogerwerf, R., de Bruijne, J. H. J., Brown, A. G. A., & Blaauw, A. 1999, *AJ*, 117, 354
- Drake, J. J. et al. 1996, *ApJ*, 469, 828
- Durney, B. R., De Young, D. S., & Roxburgh, I. W. 1993, *Sol. Phys.*, 145, 207
- Fleming, T. A., Giampapa, M. S., & Schmitt, J. H. M. M. 2000, *ApJ*, 533, 372
- Gehrels, N. 1986, *ApJ*, 303, 336
- Giampapa, M. S., Rosner, R., Kashyap, V., Fleming, T. A., Schmitt, J. H. M. M., & Bookbinder, J. A. 1996, *ApJ*, 463, 707
- Imanishi, K., Koyama, K., & Tsuboi, Y. 2001, *ApJ*, in press

- Mewe, R., Gronenschild, E. H. B. M., & van den Oord, G. H. J. 1985, *A&AS*, 62, 197
- Montmerle, T., Grosso, N., Tsuboi, Y., & Koyama, K. 2000, *ApJ*, 532, 1097
- Motte, F., André, P., & Neri, R. 1998, *A&A*, 336, 150
- Mushotzky, R. F., Cowie, L. L., Barger, A. J., & Arnaud, K. A. 2000, *Nature*, 404, 459
- Neuhäuser, R. & Comerón, F. 1998, *Nature*, 282, 83
- Neuhäuser, R. et al. 1999, *A&A*, 343, 883
- Rutledge, R. E., Basri, G., Martin, E. L., & Bildsten, L. 2000, *ApJ*, 538, L141
- Vaiana, G. S. & Rosner, R. 1978, *ARA&A*, 16, 393
- Weisskopf, M. C., O'dell, S. L., & van Speybroeck, L. P. 1996, *Proc. SPIE*, 2805, 2
- Willing, B. A., Greene, T. P., & Meyer, M. R. 1999, *AJ*, 117, 469

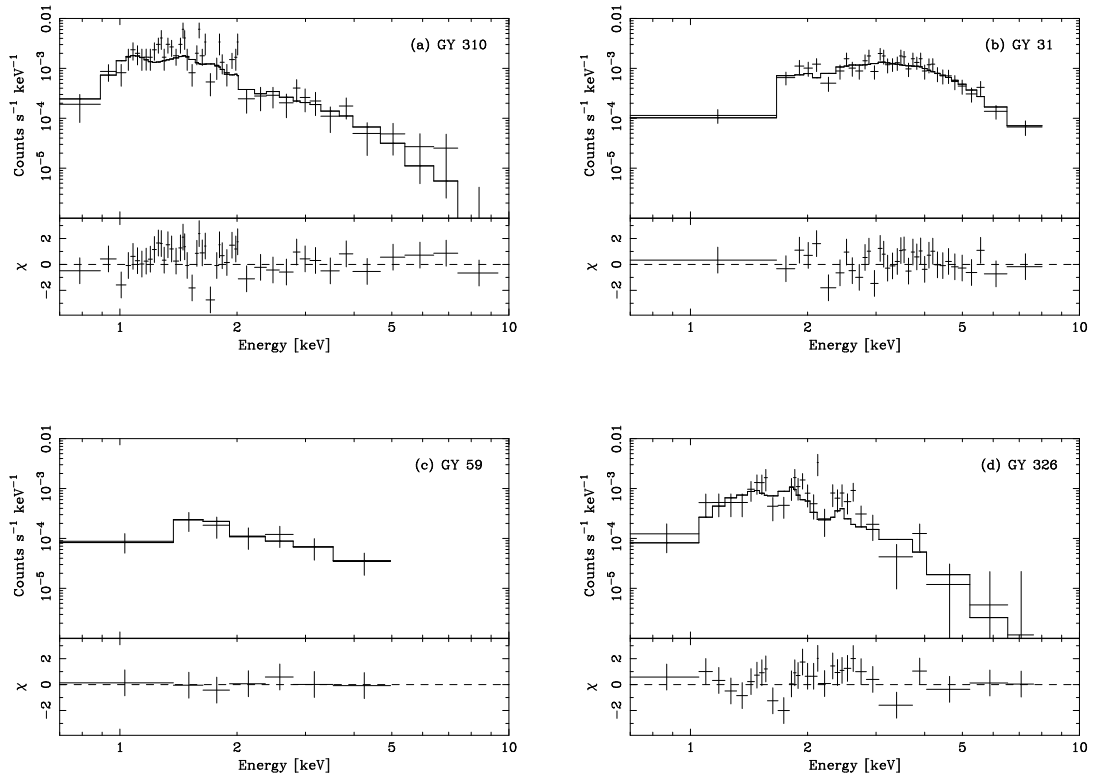


Fig. 1.— Spectra of (a) GY 310, (b) GY 31, (c) GY 59, and (d) GY 326. The upper panels show data points (crosses) and the best-fit model (solid line), while the lower panels are the data residuals from the best-fit model.

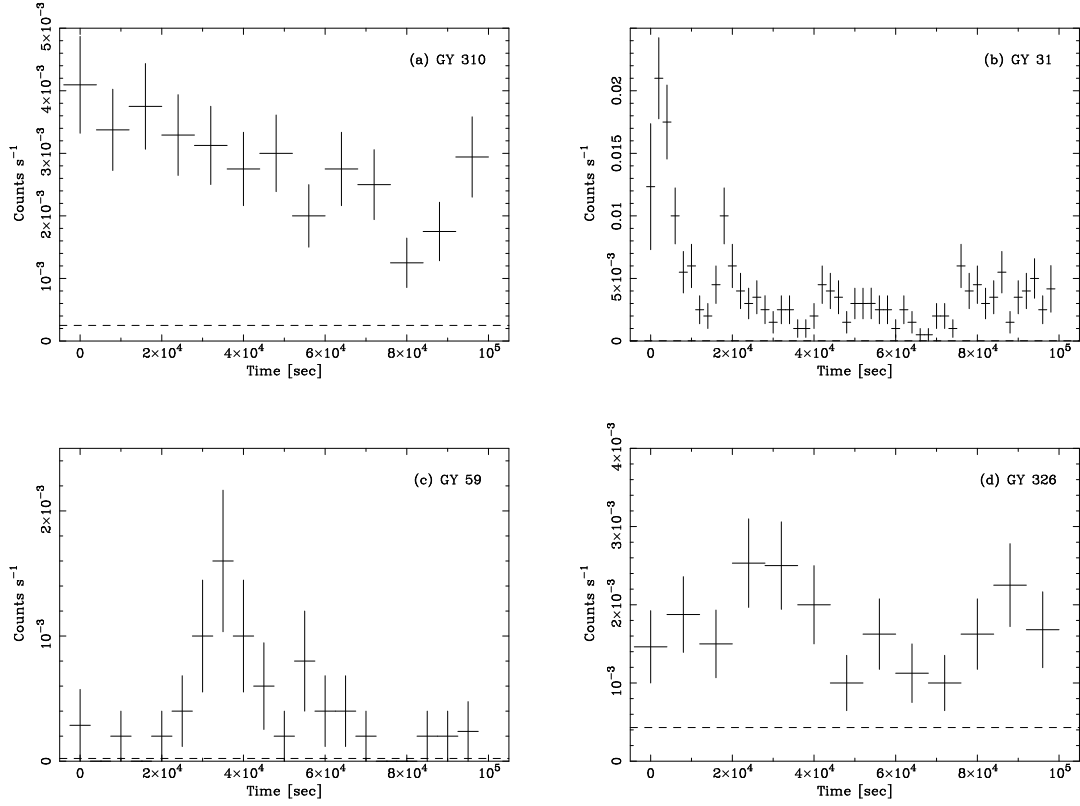


Fig. 2.— Light curves of (a) GY 310, (b) GY 31, (c) GY 59, and (d) GY 326 in the 0.5–9.0 keV band. The background level is shown by the dashed line. For GY 31, the background line ($\sim 2 \times 10^{-5}$ counts s^{-1}) overlaps with the bottom solid line.

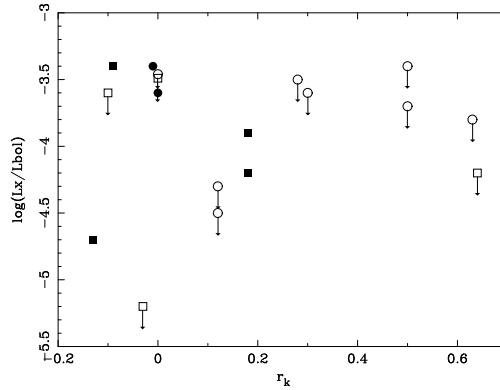


Fig. 3.— Plots of the excess emission at K -band (r_k) and the luminosity ratio between X-ray and bolometric (L_X/L_{bol}). Circles and squares represent BDs and CBDs, respectively. X-ray detection and non-detection are indicated by filled and open symbols, respectively. Arrows indicate the upper limits. GY 31 and GY 163 are not included in this figure because no r_k value has been obtained.

TABLE 1
LOG OF THE *Chandra* ACIS-I OBSERVATIONS ON THE ρ OPH CLOUD CORES

| Obs.ID | Sequence ID | Date | R.A. ^a (J2000) | Dec. ^a (J2000) | Exposure (ks) |
|--------|-------------|----------------|--|------------------------------|------------------|
| 1 | 200060 | 2000 Apr 13–14 | 16 ^h 27 ^m 18 ^s .1 | −24°34′21″.9 | 100.6 |
| 2 | 200062 | 2000 May 15–17 | 16 ^h 26 ^m 35 ^s .3 | −24°23′12″.9 | 96.4 |

^aThe position of the telescope optical axis.

TABLE 2
BONA-FIDE AND CANDIDATE BROWN DWARFS IN THE ρ OPH CLOUD CORES

| Name | Sp. type ^a | ID ^b | R.A. ^c (J2000) | Dec. ^c (J2000) | offset ^d ($''$) | PSF ^e ($''$) | X-ray counts ^f | | | 1 − CL ^g | L_X ^h (10 ²⁸ ergs s ^{−1}) | log(L_X/L_{bol}) | Ref. |
|-----------------------------|-----------------------|-----------------|------------------------------------|-------------------------------------|---------------------------------|------------------------------|---------------------------|-----|-----|----------------------------|--|-----------------------------|------|
| Soft | Hard | BGD | | | | | | | | | | | |
| Brown Dwarf (BD) | | | | | | | | | | | | | |
| CRBR 14 | M7.5 | 2 | ... | ... | ... | 5.7 | 3 | 2 | 0.5 | ND (S) | <0.55 | < −4.3 | 1 |
| GY 10 | M8.5 | 2 | ... | ... | ... | 3.2 | 2 | 0 | 0.2 | ND (S) | <0.48 | < −4.5 | 1 |
| GY 11 | M6.5 | 2 | ... | ... | ... | 3.3 | 1 | 1 | 0.2 | ND (T) | <0.12 | < −3.8 | 1, 2 |
| CRBR 31 | M6.7 | 2 | ... | ... | ... | 7.1 | 0 | 2 | 0.9 | ND (H) | <0.56 | < −3.6 | 2 |
| GY 64 | M8 | 2 | ... | ... | ... | 3.7 | 1 | 0 | 0.2 | ND (S) | <0.93 | < −3.5 | 1, 2 |
| GY 141 | M8 | 1 | ... | ... | ... | 9.0 | 7 | 1 | 1.5 | 8.0×10 ^{−4} (S) | 0.25 | −3.6 | 2 |
| | | 2 | ... | ... | ... | 22.3 | 11 | 23 | 8.6 | ND (S) | <0.33 | < −3.5 | |
| GY 202 | M7 | 1 | ... | ... | ... | 9.4 | 2 | 4 | 1.6 | ND (S) | <1.2 | < −3.7 | 1 |
| | | 2 | ... | ... | ... | 16.8 | 3 | 9 | 4.9 | ND (S) | <2.0 | < −3.4 | |
| GY 310 | M8.5 | 1 | 27 ^m 38 ^s .6 | 38 [′] 39 ^{′′} .1 | 1.3 | 9.2 | 182 | 59 | 1.5 | <1.0×10 ^{−15} (T) | 9.3 | −3.4 | 1 |
| Candidate Brown Dwarf (CBD) | | | | | | | | | | | | | |
| CRBR 15 | M5 | 2 | ... | ... | ... | 4.2 | 2 | 1 | 0.3 | ND (S) | <1.1 | < −4.2 | 1 |
| GY 5 | M7 | 2 | ... | ... | ... | 4.7 | 2 | 1 | 0.4 | ND (S) | <0.16 | < −5.2 | 1 |
| GY 31 | M5.5 | 2 | 26 ^m 25 ^s .2 | 23 [′] 25 ^{′′} .7 | 0.2 | 2.5 | 41 | 350 | 0.1 | <1.0×10 ^{−15} (T) | 93 | −3.5 | 1 |
| GY 37 | M6 | 2 | 26 ^m 27 ^s .8 | 26 [′] 43 ^{′′} .9 | 0.8 | 4.2 | 7 | 5 | 0.3 | 3.7×10 ^{−8} (S) | 0.59 | −4.2 | 1 |
| GY 59 | M6 | 2 | 26 ^m 31 ^s .4 | 25 [′] 32 ^{′′} .2 | 0.7 | 2.6 | 17 | 22 | 0.1 | <1.0×10 ^{−15} (T) | 2.6 | −3.9 | 1 |
| GY 84 | M6 | 2 | ... | ... | ... | 1.9 | 2 | 2 | 0.1 | 1.3×10 ^{−4} (T) | 0.85 | −4.7 | 1 |
| GY 163 | M2.5 | 1 | ... | ... | ... | 12.4 | 5 | 12 | 2.8 | ND (T) | <12 | < −3.8 | 1 |
| | | 2 | ... | ... | ... | 11.9 | 3 | 7 | 2.4 | ND (S) | <10 | < −3.8 | |
| GY 218 | M4.0 | 1 | ... | ... | ... | 7.2 | 2 | 3 | 0.9 | ND (S) | <0.45 | < −3.6 | 2 |
| CRBR 67 | M4.4 | 1 | ... | ... | ... | 3.2 | 0 | 0 | 0.2 | ND (−) | <0.31 | < −3.5 | 2 |
| GY 326 | M4 | 1 | 27 ^m 42 ^s .8 | 38 [′] 51 ^{′′} .1 | 1.5 | 11.4 | 67 | 65 | 2.3 | <1.0×10 ^{−15} (T) | 28 | −3.4 | 1 |

^aSpectral type determined from the water vapor absorption.

^bObservation identification (see Table 1).

^cPosition of the identified X-ray source which is picked up with the `wavdetect` command (see §3.1). Right ascension and declination for all sources are at 16^h and -24°.

^dOffset between the IR and the X-ray sources.

^eRadius of the point-spread function.

^fX-ray counts in the soft (0.5–2.0 keV) and hard (2.0–9.0 keV) bands, and predicted background counts in the soft band within the source circle. Background counts in the hard band is ~ 3 times larger than those in the soft band.

^g CL is the confidence level of the source detection (see §3.1). Parentheses indicate the energy band in which the maximum CL value is obtained (S: 0.5–2.0 keV, H: 2.0–9.0 keV, T: 0.5–9.0 keV). ND represents non X-ray detection with $CL < 0.999$ (i.e., $1 - CL > 10^{-3}$).

^hAbsorption-corrected luminosity in 0.5–9.0 keV. The distance to each source is assumed to be 145 pc (de Zeeuw et al. 1999).

REFERENCES.—(1): Wilking et al. (1999); (2): Cushing et al. (2000)

TABLE 3
BEST-FIT PARAMETERS OF THE BRIGHTEST 4 SOURCES

| Name | kT^a (keV) | $\log(EM)^a$ (cm^{-3}) | N_H^a (10^{22}cm^{-2}) | $\chi^2/d.o.f$ |
|--------|-----------------|--------------------------------------|--|----------------|
| GY 310 | 1.7(0.9–2.2) | 51.6(51.5–52.1) | 0.8(0.5–1.5) | 57.8/44 |
| GY 31 | 2.2(1.7–2.9) | 52.6(52.4–52.8) | 5.9(5.1–7.2) | 25.1/33 |
| GY 59 | 2.5(>1.0) | 51.0(50.6–51.7) | 1.4(0.5–3.0) | 0.556/4 |
| GY 326 | 0.9(0.7–1.2) | 52.1(51.7–52.4) | 2.3(1.6–3.0) | 34.8/28 |

^aParentheses indicate the 90% confidence limits.